

## Article

# Seismic Performance of a Novel Precast Beam-Column Joint Using Shape Memory Alloy Fibers-Reinforced Engineered Cementitious Composites

Weihong Chen <sup>1</sup>, Kai Feng <sup>1</sup> , Ying Wang <sup>1,\*</sup>, Shuangshuang Cui <sup>2</sup> and Yiwang Lin <sup>1</sup><sup>1</sup> College of Civil Engineering, Fuzhou University, Fuzhou 350108, China<sup>2</sup> School of Civil Engineering, Fujian University of Technology, Fuzhou 350118, China

\* Correspondence: wangying763@fzu.edu.cn

**Abstract:** A novel precast beam–column joint using shape memory alloy fibers-reinforced engineered cementitious composites (SMA-ECC) was proposed in this study to achieve self-repairing of cracks and internal damage after an earthquake. Three large-scale beam–column joints were tested under displacement reversals, including one monolithically cast conventional concrete joint, one engineered cementitious composites (ECC) reinforced precast concrete joint, and one SMA-ECC reinforced precast concrete joint. Failure mode, crack pattern, hysteretic behavior, stiffness degradation, displacement ductility, and energy dissipation capacity were compared and evaluated through a cyclic loading test. The test results showed that the ECC-based (ECC, SMA-ECC) precast joints have equivalent seismic properties to the monolithically cast concrete joint. ECC-based joints enhanced the ductility and energy dissipation capacity of the joint and, remarkably, reduced crack width. The SMA-ECC reinforced joint also exhibited instant self-healing in terms of the closure of small cracks after unloading. The self-healing performance was further evaluated through ultrasonic pulse tests, with the results showing that the use of SMA-ECC material was efficient in reducing the internal damage of beam–column joints after an earthquake.

**Keywords:** beam–column joints; seismic performance; self-repairing; engineered cementitious composites; ultrasonic pulse test



**Citation:** Chen, W.; Feng, K.; Wang, Y.; Cui, S.; Lin, Y. Seismic Performance of a Novel Precast Beam-Column Joint Using Shape Memory Alloy Fibers-Reinforced Engineered Cementitious Composites. *Buildings* **2022**, *12*, 1404. <https://doi.org/10.3390/buildings12091404>

Academic Editors: Radu Vacareanu and Florin Pavel

Received: 28 July 2022

Accepted: 2 September 2022

Published: 7 September 2022

**Publisher's Note:** MDPI stays neutral with regard to jurisdictional claims in published maps and institutional affiliations.



**Copyright:** © 2022 by the authors. Licensee MDPI, Basel, Switzerland. This article is an open access article distributed under the terms and conditions of the Creative Commons Attribution (CC BY) license (<https://creativecommons.org/licenses/by/4.0/>).

## 1. Introduction

In recent years, precast concrete (PC) structures have been extensively applied in many countries and regions because of their promising quality, lower cost, and relatively short construction time compared to cast-in-place reinforced concrete (RC) structures [1]. However, PC frame structures are vulnerable to seismic load due to their compromised structural integrity of beam–column joints [2]. It is reported that structures with precast RC frames as the lateral force resisting system perform poorly in strong earthquakes [3,4]. For example, the collapse of many precast structures was triggered by severe damages of beam–column joints during the 12 May 2008 Wenchuan Earthquake [5] and the 17 August 1999 Marmara Earthquake [6].

The seismic performance of structures with precast RC frames depends heavily on the behavior of beam–column joints, which are the most critical yet weakest component of the frame [7]. A beam–column joint with good seismic performance could effectively transfer internal forces. It should also be able to dissipate enough energy and be sufficiently ductile to withstand large displacement reversals during strong earthquakes. Due to the intrinsic brittleness and low tensile strength of concrete, it is hard to achieve the abovementioned requirement of a beam–column joint [8]. Reinforcing bars may not be fully utilized during earthquakes because of the deformation incompatibility between brittle concrete and ductile reinforcing bars. In addition to the above-mentioned difficulties, for PC joints, the connections between the precast beam and column weaken the integrity of

the structure, since the casting interface of PC joints is more vulnerable to earthquakes. To improve the load-bearing capacity and seismic performance of RC frames, the RC jacketing method is extensively used for strengthening RC joints. It can effectively enhance the strength, stiffness, and ductility of concrete members by increasing section area in damaged columns [9]. However, larger member size may compromise the structural serviceability.

The application of high-performance fiber-reinforced cementitious composite (HPFRCC) materials has thrived during the past few decades. Engineered cementitious composites (ECC) is one novel type of HPFRCC material with tensile strain-hardening behavior, multi-cracking properties, and ultra-ductility [10,11], which can significantly improve the energy absorption capacity and damage resistance under seismic loads. Ultra-high-performance concrete (UHPC) is a type of fiber-reinforced concrete material that exhibits high compressive strength (at least 120 MPa) and tensile strength (at least 7 MPa) [12]. It has been demonstrated by previous research that HPFRCC is a class of promising building materials for earthquake-resistant structures because of its improved compression and tension properties [13]. In contrast to conventional concrete, which normally has a compressive fracture energy of 10 to 25 N/mm, ECC and UHPC have been found to have a compressive fracture energy ranging from 53 to 180 N/mm [14,15]. Kesner et al. [16] reported that cyclic tension behavior follows the monotonic tension curve for PVA-ECC without compression softening. In contrast, Khlef et al. [17] found that for HPFRCC with hybrid PVA and steel fibers, the tensile strength and flexural toughness decrease with increased cyclic loading.

Many research works have investigated the seismic performance of beam–column joints using different HPFRCC materials, such as steel fiber-reinforced concrete (SFRC) [18,19], UHPC [20], and ECC [21–23]. These studies showed that the use of SFRC in the joint zone can enhance the shear strength, while the application of UHPC can significantly improve the bearing capacity and shear resistance and reduce the amount of reinforcement in the joint zone. Gou et al. [24] proposed a novel type of precast beam–column joint (PJ) comprising concrete columns, U-shaped low-shrinkage ECC (LSECC) beam shells, and joint core area with LSECC. After five LSECC/RC joints with different reinforcement details were tested under cyclic loading, it was found that LSECC/RC joints can effectively simplify the reinforcement details in a joint zone. In addition, the seismic performance of ECC joints is also affected by fiber types to some extent. Ismail et al. [25] found that, at the same fiber volume content, the ductility and energy dissipation of the ECC joint with steel fibers are 29% and 27% higher, respectively, than those of PVA-ECC joint. Although the above joints show desirable seismic behavior during an earthquake, severe damage and larger residual deformation in the joint zone are inevitable under larger displacement reversals, resulting in high maintenance costs and efforts after strong earthquakes.

Recently, the concept of intelligent structural systems has attracted attention worldwide. The intelligent system is a new type of structural system that can automatically modify structural characteristics and restore structural function after disastrous incidents, hence improving structural serviceability and reducing the retrofitting cost [26,27]. This concept also facilitates the implementation of the main sustainable development goals (SDG) proposed by the United Nations Agenda. For example, after the 2009 L'Aquila Earthquake, the actual repair costs on drift sensitive members highly ranged from 70~90% of total building repair costs [28]. The performance of the SR 99 Alaskan Way Viaduct south access connection (AWV-SAC) bridge scaled columns using an intelligent composite system combining two innovative materials was evaluated [29]. This intelligent system provides good post-earthquake performance with limiting residual deformation and eliminating spalling damage, which is of benefit to reduce the economic and social costs of need repair and rehabilitation after an earthquake. In particular, smart materials play a key role in intelligent systems by providing important functions such as sensing, actuation, and autogenous healing. Shape memory alloys (SMAs) are a class of smart materials that exhibit unique super-elasticity and shape memory effect, and have a recoverable strain up to 6~8% [27], with their great controlling effect extensively used for energy dissipation [30]. With the development SMAs and ECCs, important structural members have been designed

based on intelligent composite systems combining SMAs and ECCs. For the seismic performance of structural members, beams [31,32], bridge columns [33–35], and beam–column joints [36] have been investigated. These results showed that SMA bars can significantly enhance the self-centering capacity, while the use of ECC can improve the ductility and energy dissipation capacity. However, the members reinforced with SMA bars and ECCs performed poorly on strength and initial stiffness compared to RC members.

Shape memory alloy fibers-reinforced engineered cementitious composites (SMA-ECC) is a novel, self-healing concrete material with outstanding energy dissipation capacity, multi-microcracks distributed characteristics, and self-healing properties [37–40]. Ali et al. [38] studied the behavior of SMA-ECC under impact loads through drop weight impact tests, and found that SMA-ECC materials exhibited superior tensile properties and impact resistance. The authors of [39,40] evaluated the self-healing performance of SMA-ECC through four-point bending tests and ultrasonic pulse tests. According to the test results, SMA fibers could effectively close micro-cracks, while SMA-ECC specimens with 1.0% of SMA fiber content exhibited satisfactory crack-healing capacity and damage-repairing capacity, which could potentially reduce the maintenance costs of post-earthquake structures. Thus, it has been demonstrated by the previous research that SMA-ECC is a very promising material for the application of critical structural members while achieving SDG in terms of performance, safety, and economy.

This paper proposed a novel PJ using SMA-ECC materials in the joint core zone aiming to reduce joint zone damage and achieve self-repairing of cracks and internal damage after an earthquake. Three large-scale beam–column joints, including one monolithically cast joint and two precast joints, were fabricated and tested by cyclic loading tests. The effects of material type (concrete, ECC, and SMA-ECC) in the joint zone on seismic performance and self-healing performance were investigated. The test results were summarized and discussed. The self-healing performance in terms of crack healing and internal damage repairing was also evaluated through acoustic tests. The precast beam–column joint reinforced with SMA-ECC materials exhibited better performance in energy dissipation and crack healing compared to the monolithically cast RC joint.

## 2. Experimental Program

### 2.1. Specimen Design

Three beam–column joints were designed, including one cast-in-place joint (J-RC) and two precast joints (PJ-ECC and PJ-SMA-ECC), as listed in Table 1. All beam–column joint specimens were designed following the principles of “strong column–weak beam” and “strong joint–weak member” as suggested in the Code for Seismic Design of Buildings [41]. Specifically, the flexural capacity ratio of column-to-beam was designed to exceed 1.3, so that the plastic hinges would form at the beam ends. The shear capacity of the joint was calculated according to ACI 352R-02 [42] (Equations (1)–(3)):

$$\phi v_n \geq v_u \quad (1)$$

$$v_n = \frac{1}{12} \gamma \sqrt{f'_c} \quad (2)$$

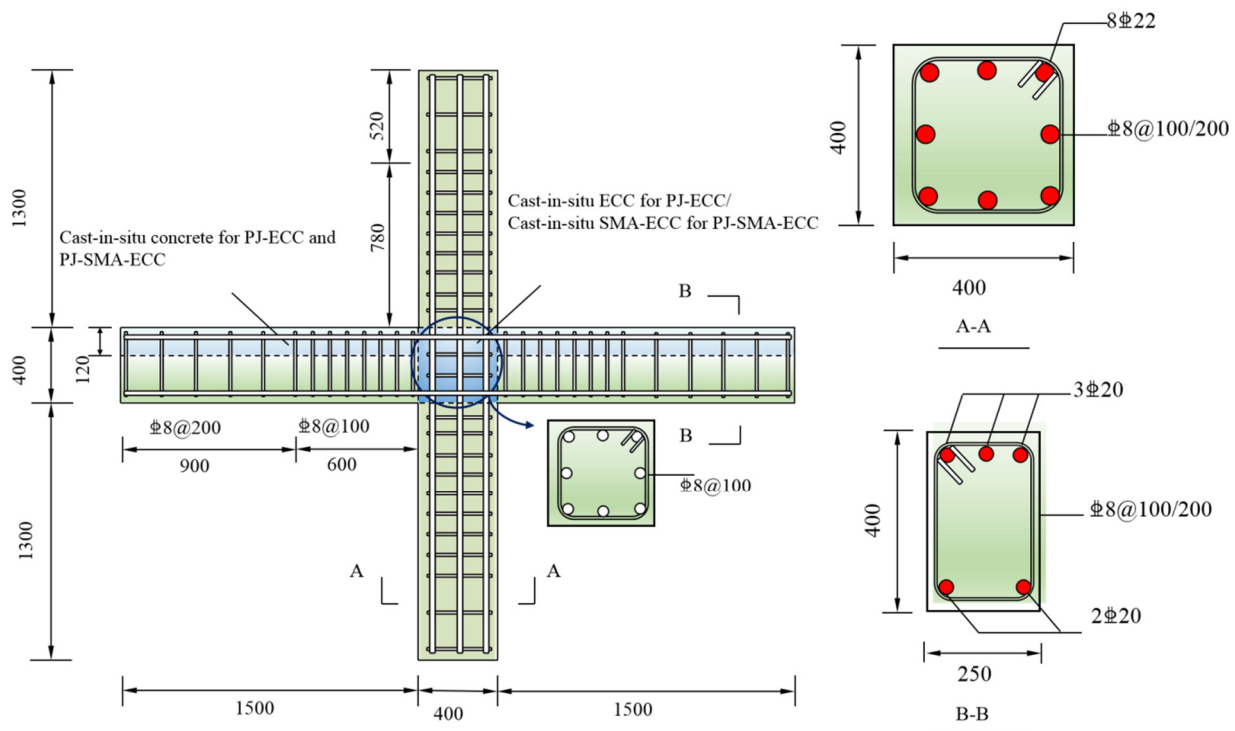
$$v_u = \frac{\alpha (f_{y1} A_{s1} + f_{y2} A_{s2}) - V_{col}}{b_j h_c} \quad (3)$$

where  $\phi$  is taken as 0.85,  $v_n$  is the nominal shear stress,  $\gamma$  is taken as 15 for beam–column joint,  $f'_c$  is the nominal compressive strength,  $b_j$  is the effective joint width,  $h_c$  is the depth of the column in the direction of joint shear,  $A_{s1}$  and  $A_{s2}$  are the areas of compression and tension reinforcement,  $f_{y1}$  and  $f_{y2}$  are the yield strengths of compressive and tensile reinforcement,  $V_{col}$  is the shear in the column, and  $\alpha$  is the stress multiplier for longitudinal reinforcement at the joint–member interface (equal to 1.25).

**Table 1.** Specimen beam–column joint details.

Specimen	Type	Axial Compressive Ratio	Material in Joint Zone
J-RC	monolithic	0.2	Concrete
PJ-ECC	precast	0.2	ECC
PJ-SMA-ECC	precast	0.2	SMA-ECC

All the specimens shared the same geometry and reinforcement layout, as shown in Figure 1. The cross-section size of the beam was 250 mm × 400 mm. The beam was longitudinally reinforced with three  $\phi 20$  top steel bars and two  $\phi 20$  bottom steel bars, and transversely reinforced with two legs of  $\phi 8$  steel bars (spacing of 100 mm or 200 mm). The cross-section size of the column was 400 mm × 400 mm. The column was longitudinally reinforced with eight  $\phi 22$  steel bars, and the arrangement of the stirrups was similar to the beams. Additionally, the stirrups in the joint zone were identical to those in the column with two legs of  $\phi 8$  steel bars with a spacing of 100 mm.

**Figure 1.** Details of joint specimens (unit: mm).

The difference between these specimens were the casting procedure and material in the joint zone. Specimen J-RC was cast monolithically with ordinary concrete. The columns and partial beams of Specimens PJ-ECC and PJ-SMA-ECC were pre-casted, while the rest of the beams were cast in the field with ordinary concrete, as shown in Figure 1. The joint zone of Specimens PJ-ECC and PJ-SMA-ECC was cast in the field with ECC and SMA-ECC, respectively. The interfaces between precast concrete and cast-in-place SMA-ECC or ECC were roughened using artificial chiseling to improve the integrity of precast joints. The precast RC column of the upper story was connected with the longitudinal bars extended from the joint by grout sleeve connections, which were widely used in precast structures to improve bond and structural integrity.

## 2.2. Specimen Fabrication

In relation to the limitations of practical construction conditions and the convenience of specimen fabrication, the horizontal pouring method was adopted in this study. The fabrication processes of the proposed joint were as follows: (1) The lower precast column

was prefabricated and placed in position; (2) The precast beams were assembled in the wood formwork; (3) The longitudinal reinforcements in the top of the beam and the stirrups in the joint zone were placed; (4) The upper precast column was assembled by inserting bars of the lower precast column to the embedded grout sleeves in the upper column, as shown in Figure 2; (5) Grouting the grout sleeves of the column joints; (6) The joint zone and the top of the precast beam were cast in the field with ECC/SMA-ECC and ordinary concrete, respectively.

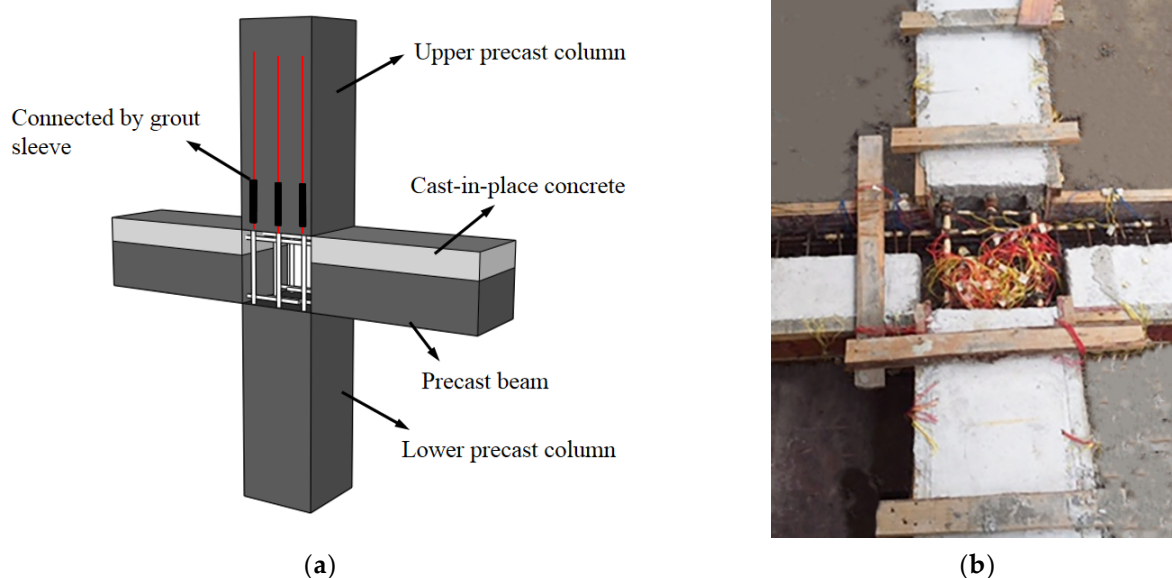


**Figure 2.** The fabrication of the precast joint. (a) Schematic diagram; (b) Photo.

### 2.3. Materials Properties

Three types of materials were used in this experimental program: ordinary concrete, ECC composite, and SMA-ECC composite. The mix proportions of the ECC and SMA-ECC materials are listed in Table 2, with the mechanical properties of PVA and SMA fibers shown in Table 3. The tensile strength of PVA and SMA fibers were 1560 MPa and 895 MPa, respectively. The diameter and length of SMA fiber is 0.6 mm and 16 mm, respectively. In this study, a heat treatment process was used to improve the super-elastic property of SMA fiber as previously described by the authors [39]. The mix proportion of concrete with a nominal compressive strength of 40 MPa is tabulated in Table 4.

**Table 2.** Mix proportions of SMA-ECC and ECC (weight proportion).

	Cement	Fly Ash	Slag Powder	Quartz Sand	Water	Water Reducer	PVA Fiber (V%)	SMA Fiber (V%)
SMA-ECC	0.15	0.7	0.15	0.4	0.25	0.003	1.70	1.00
ECC	0.15	0.7	0.15	0.4	0.25	0.003	1.70	0.00

**Table 3.** Mechanical properties of PVA and SMA fibers.

Type	Diameter (mm)	Length (mm)	Tensile Strength (MPa)	Elastic Modulus (GPa)	Density (kg/m <sup>3</sup> )
PVA	0.04	12	1560	42.8	1300
SMA	0.6	16	895	41	6450

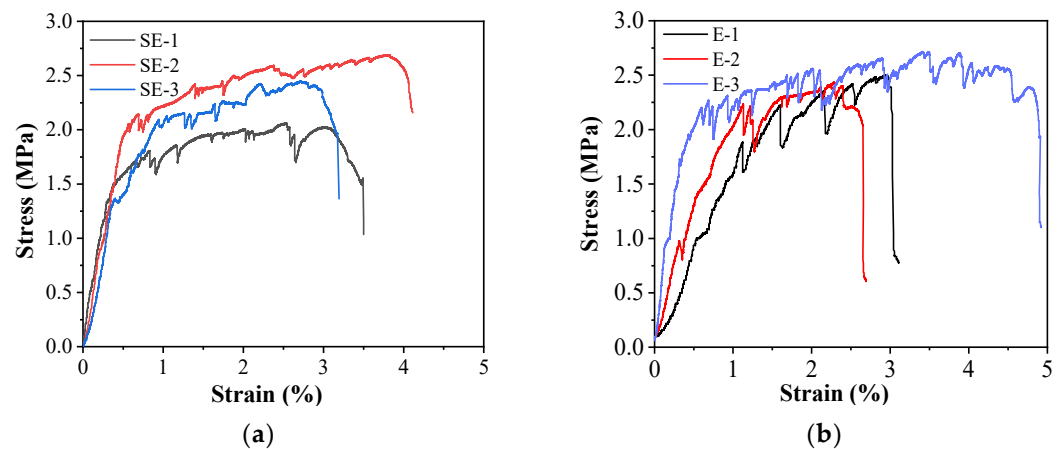
**Table 4.** Mix proportions of concrete.

Material	Water	Cement	Sand	Coarse Aggregate	Fly Ash	HRWRA
Content (kg/m <sup>3</sup> )	163	347	693	1130	82	9.9
Weight proportion (%)	0.47	1.00	2.00	3.26	0.24	0.029

The compressive strength of SMA-ECC, ECC, and concrete was determined by conducting axial compressive tests on 150 mm × 150 mm × 150 mm cubes following GB/T 50081-2019 [43], with the average results shown in Table 5. Direct tensile tests were conducted on SMA-ECC and ECC using bone-shaped specimens with a dimension of 355 mm × 100 mm × 50 mm. Each type of material includes three specimens. The tensile stress–strain curves of SMA-ECC and ECC are shown in Figure 3, with the ultimate tensile strain of both specimens exceeding 2.6% and the tensile strength both exceeding 2.4 MPa. The tensile test results of SMA-ECC and ECC are listed in Table 6. The grade of the reinforcing bars was HRB400. Material properties were tested according to GB/T 228.1-2010 [44], with the test results tabulated in Table 7.

**Table 5.** Compressive strength of concrete, ECC, and SMA-ECC.

Scheme 43.	Strength of Concrete (MPa)	Strength of ECC (MPa)	Strength of SMA-ECC (MPa)
Precast beam	43.4	—	—
Precast column	43.4	—	—
Cast-in-place zone	42.1	43.7	40.2

**Figure 3.** The tensile stress–strain curves of materials. (a) SMA-ECC; (b) ECC.**Table 6.** Tensile test results of ECC and SMA-ECC.

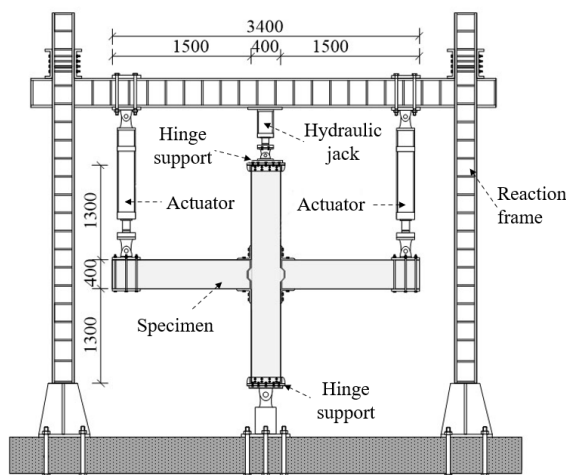
Material	Tensile Specimen	Tensile Strength (MPa)	Ultimate Tensile Strain (%)
SMA-ECC	SE-1	2.06	3.50
	SE-2	2.69	4.07
	SE-3	2.44	3.18
	Average	2.40	3.58
ECC	E-1	2.48	3.03
	E-2	2.42	2.65
	E-3	2.68	—
	Average	2.53	2.84

**Table 7.** Material properties of the reinforcing bars.

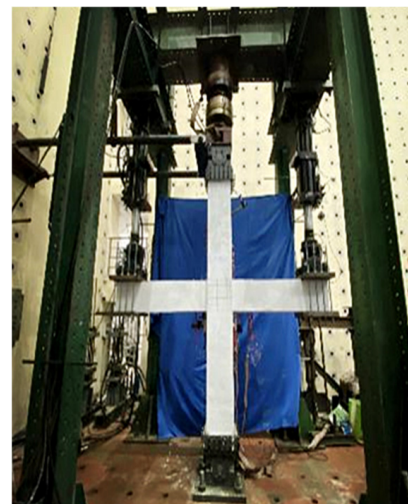
Scheme	Diameter (mm)	Yield Strength (MPa)	Ultimate Strength (MPa)	Elastic Modulus (GPa)	Elongation (%)
Stirrup bar	8	436	635	201	14.66
Longitudinal bars	20	435	629	211	14.11
	22	432	621	199	13.74

#### 2.4. Test Setup and Loading Procedure

Figure 4 shows the typical test setup. Both the top and bottom of the columns were attached to hinges to create inflection points at a middle-height position of the column. The top hinge was attached to the loading frame, while the bottom hinge was anchored to the reaction floor. Each beam end was attached to a 500 kN vertical MTS hydraulic actuator. Two actuators simultaneously caused opposite displacements, i.e., one upward and the other downward. A 5000 kN hydraulic ram was connected to the column top to apply a constant axial load.



(a) Elevation



(b) Photo

**Figure 4.** Test setup shown as a (a) diagram and (b) photograph.

The applied loads were measured with load cells placed between the column top and the hydraulic ram. The load and displacement of the beam ends were measured by load cells and displacement transducers, respectively. Strain gauges were attached to the longitudinal steel bars and stirrups in the joint region to monitor strain change during the test.

This test was displacement-controlled following the loading protocol recommended by the Specification for Seismic Test of Building [45], as shown in Figure 5. The displacement increment was 2 mm before yielding and each displacement target was not repeated. The displacement increment was set as  $\Delta_y$  after yielding and each displacement target was repeated twice, where  $\Delta_y$  was the yield displacement. The test was terminated when the applied load reduced to 85% of the peak load.

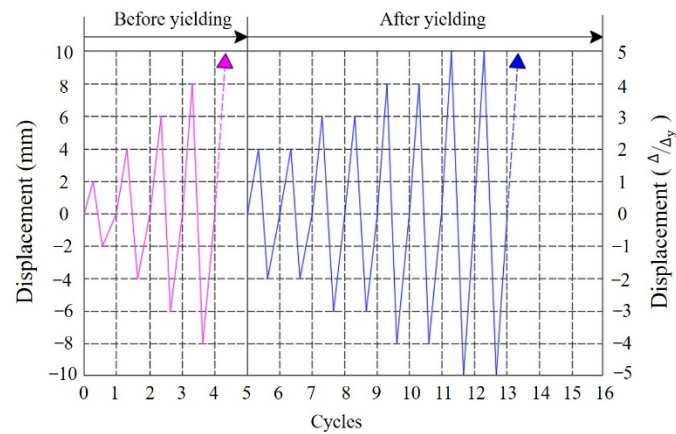


**Figure 5.** Loading procedure in the test.

### 3. Test Results

#### 3.1. General Observations

Figure 6 displays the failure mode of each specimen. The failure mechanism of “strong joint–weak member” and “strong column–weak beam” was achieved by the formation of flexural hinges at the beam ends while limited shear cracks were generated in the joint zone. The following section describes observations of each specimen during the testing process.

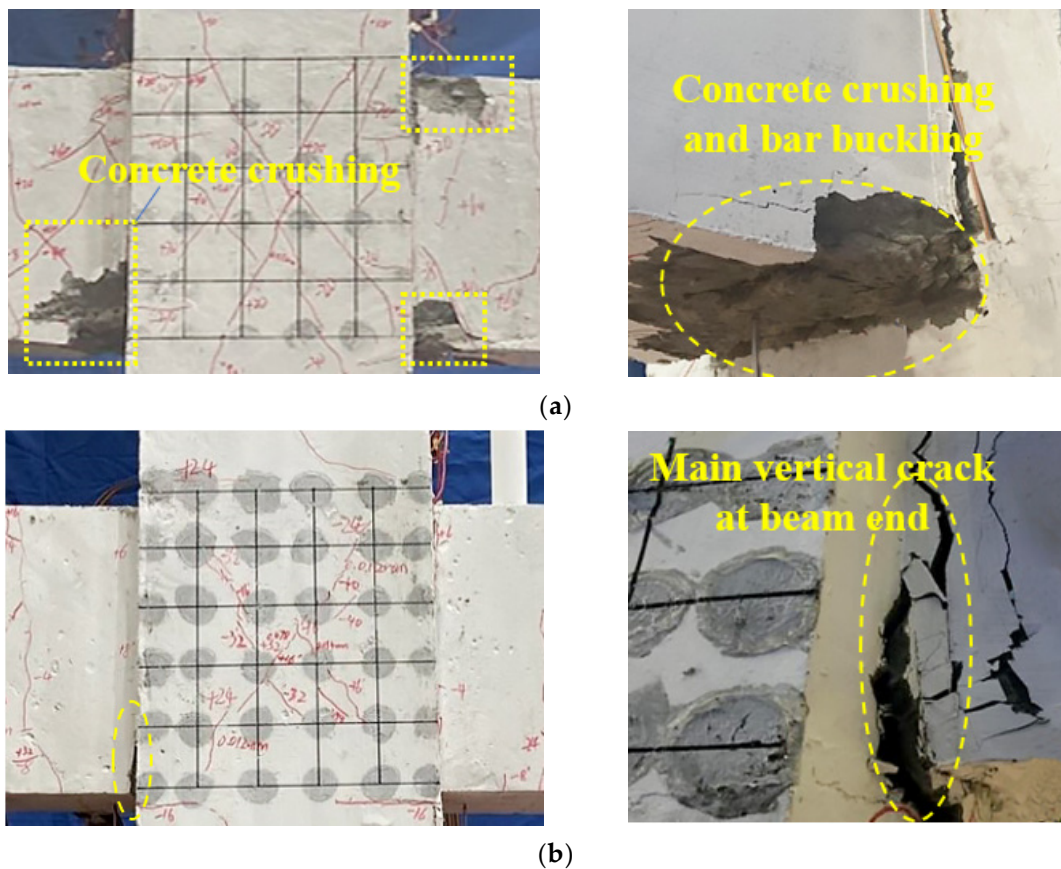


**Figure 6.** Cont.

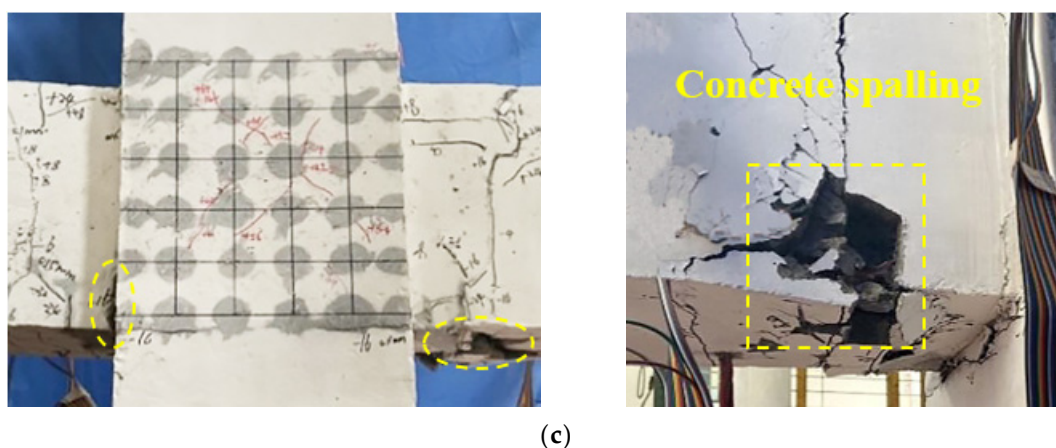


**Figure 6.** Failure modes of the three specimens. (a) Specimen J-RC; (b) Specimen PJ-ECC; (c) Specimen PJ-SMA-ECC.

**Specimen J-RC:** The initial flexural crack with a width of 0.032 mm was developed at the bottom of the left beam near the joint when the applied displacement was 4 mm. More cracks gradually developed and propagated toward the neutral axis of the beam with increasing load, with cracks observed on both the top and bottom of the beams when the load was reversed. The top reinforcement of the right beam yielded at the moment the displacement reached 10 mm ( $\Delta_y$  equals 10 mm). In the loading cycle of  $2\Delta_y$ , the first diagonal crack with a width of 0.026 mm was formed in the joint zone. As loading displacement reached  $4\Delta_y$ , concrete at the bottom of the beams began to spall off. In addition, diagonal cracks in the joint zone gradually extended with a crack width of 0.552 mm. The specimen failed at a displacement of  $7\Delta_y$  with the formation of typical flexural plastic hinges at the beam ends: severe concrete spalling at the top and bottom of the beam end. Concrete crushing and buckling of the bottom longitudinal rebar were observed, as shown in Figure 6a.

**Specimen PJ-ECC:** The initial flexural crack with a width of 0.024 mm was observed at the top of the left beam at a loading displacement of 4 mm. More cracks gradually developed on both the top and bottom of the beams, and propagated toward the neutral axis of the beam as the loading increased. The left beam yielded at a displacement of 8 mm ( $\Delta_y$  equals 8 mm). After yielding, the top and bottom flexural cracks connected under displacement reversals. Meanwhile, a vertical crack formed at the interface between the beam and joint zone, while crack width increased with increasing load. The first diagonal crack with a crack width of 0.034 mm in the joint zone was formed at a displacement of  $2\Delta_y$ . As loading displacement reached  $3\Delta_y$ , a vertical crack quickly started to develop upward at each beam end near the joint. Finally, the crack width reached approximately 4.4 mm at a loading displacement of  $5\Delta_y$ . At a displacement of  $9\Delta_y$ , the specimen failed with a complete vertical crack at the beam–joint interface, as shown in Figure 6b. There was no concrete/ECC spalling or crushing during the test. Compared to J-RC, closely spaced small diagonal cracks were observed in the joint zone of PJ-ECC and this specimen maintained good integrity after the test stopped.

**Specimen PJ-SMA-ECC:** Initial flexural cracks with a crack width of 0.028 mm were found at the bottom of the beams near the joint at a displacement of 4 mm. Crack development was similar to Specimen PJ-ECC. This specimen yielded at a loading displacement of 8 mm ( $\Delta_y$  equals 8 mm). The first vertical crack with a width of 0.021 mm at the beam–column interface was observed at a displacement of 8 mm. Meanwhile, flexural cracks gradually increased and developed on both the top and bottom of the beam end. At a displacement of  $3\Delta_y$ , the first diagonal crack was generated in the joint zone, with a crack width of 0.023 mm. At the same time, the vertical crack at the beam–column interface developed quickly, with the crack width reaching 1.2 mm. At a displacement of  $6\Delta_y$ , the diagonal cracks in the joint zone constantly developed and formed cross cracks, while the

maximum width was 0.032 mm. At a displacement of  $8\Delta_y$ , concrete at the bottom of the right beam began to spall off. The specimen failed at a displacement of  $9\Delta_y$ , as shown in Figure 6c. Compared with specimens J-RC and PJ-ECC, fewer and shorter shear cracks were generated in the joint zone of Specimen PJ-SMA-ECC, as shown in Figure 6.

### 3.2. Crack Pattern

Figure 7 shows the crack patterns of the specimens. Flexural cracks were generated at both the top and bottom of the beam and closely spaced diagonal shear cracks were developed in the joint zone, with a crack barely observed at the column end. Compared with Specimen J-RC, the width of the diagonal shear cracks was noticeably reduced for Specimens PJ-ECC and PJ-SMA-ECC.

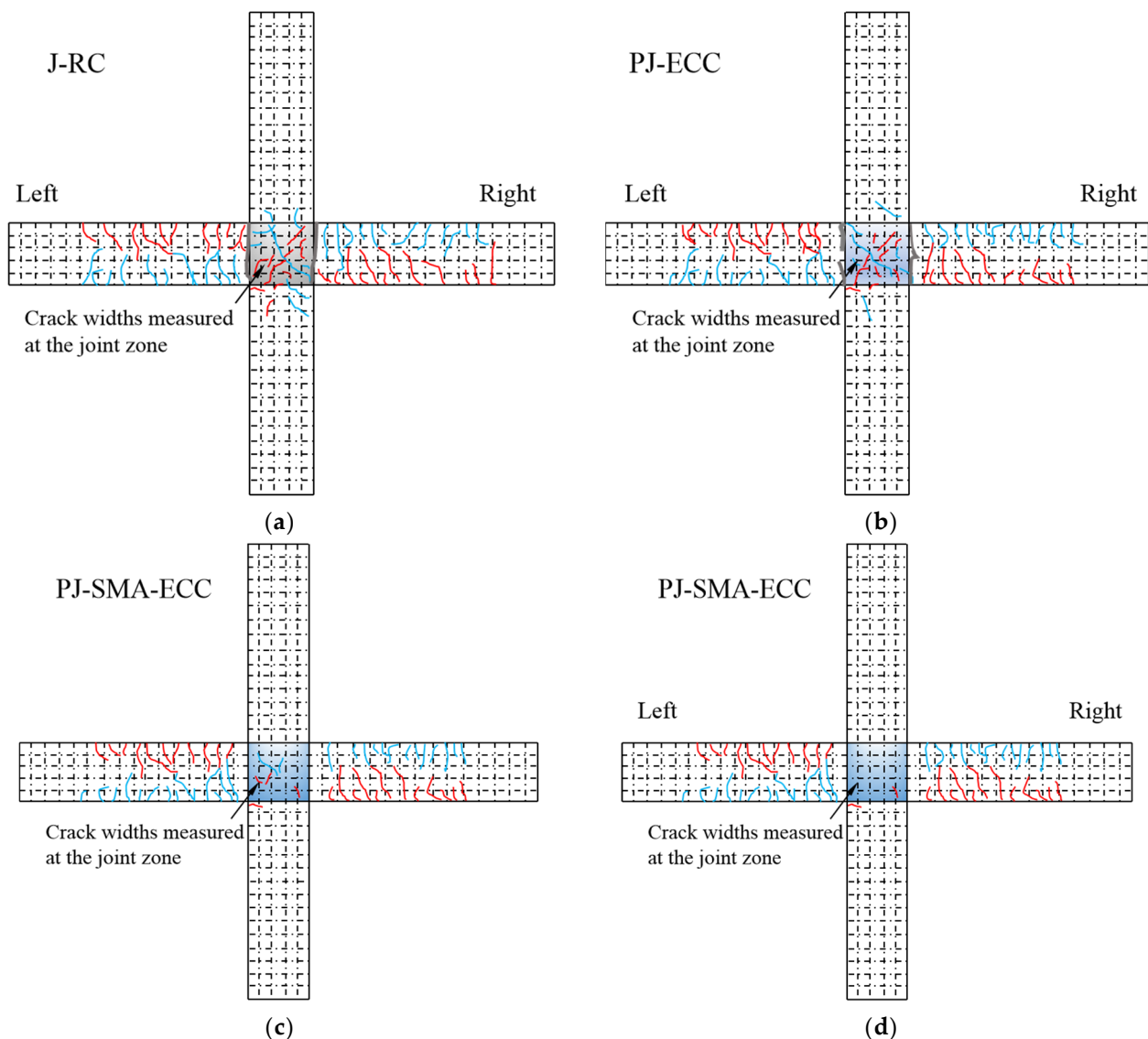


**Figure 7.** Crack patterns of specimens. (a) J-RC; (b) PJ-ECC; (c) PJ-SMA-ECC; (d) Self-healed PJ-SMA-ECC.

The crack width was measured at each predefined target displacement as mentioned in Section 2.4 using a high-precision crack gauge. The relation between measured maximum crack width in the joint zone and displacement is shown in Figure 8. In general, crack width increased with increasing displacement for all specimens. The crack width of Specimens PJ-ECC and PJ-SMA-ECC was significantly smaller than that of Specimen J-RC. For example, at a loading displacement of 40 mm, the measured maximum crack width

of Specimens J-RC, PJ-ECC, and PJ-SMA-ECC were 0.437 mm, 0.058 mm, and 0.029 mm, respectively. It can be seen that ECC-based specimens had smaller cracks under the same loading displacement compared with J-RC, which is due to the strain-hardening effect of ECC materials. It was also noticed that the crack width of Specimen PJ-SMA-ECC was smaller than that of Specimen PJ-ECC, and that is mainly due to the super-elasticity of SMA fibers which assists the SMA-ECC material of partial micro-cracks' closing ability after unloading [39]. The crack measurements in the joint zone at the final target displacement and 15 min after the test finished are tabulated in Table 8. For Specimen J-RC, 15 diagonal cracks with a maximum crack width of 1.128 mm appeared in the joint zone at the final target displacement, while for Specimen PJ-SMA-ECC, there were 8 diagonal cracks with an average crack width of 0.03 mm in the joint zone. Fifteen minutes after the test, the crack number of Specimens J-RC and PJ-ECC did not reduce, though the crack width decreased by approximately 12% and 27% of the respective values measured at the final target displacement. Compared with the other two control specimens, the crack number of Specimen PJ-SMA-ECC reduced from 8 to 1, with 7 cracks completely closed and only 1 crack, with a width of 0.011 mm, remaining in the joint zone. It can be seen that SMA-ECC materials can significantly reduce residual crack width and close mostly micro-cracks with crack width below 40  $\mu\text{m}$ .

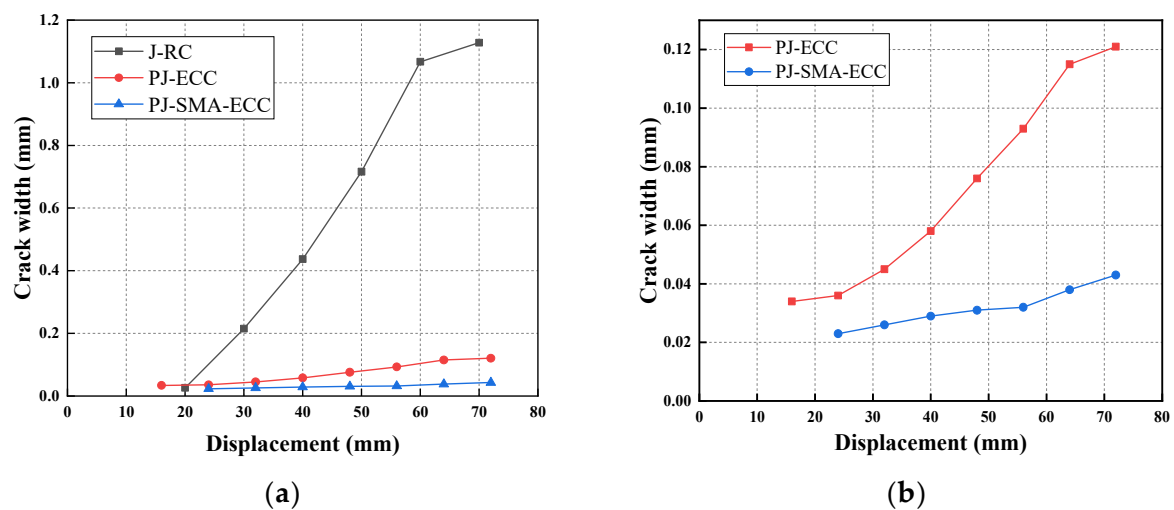


**Figure 8.** Measured maximum crack width in the joint zone vs. displacement for (a) J-RC and (b) PJ-ECC and PJ-SMA-ECC.

**Table 8.** Crack measurements in the joint zone.

	Specimen	Number of Cracks	Average Crack Width (mm)	Maximum Crack Width (mm)
The final target displacement	J-RC	15	0.652	1.128
	PJ-ECC	13	0.058	0.121
	PJ-SMA-ECC	8	0.030	0.043
15 min after the test stopped	J-RC	15	0.571	0.781
	PJ-ECC	13	0.042	0.112
	PJ-SMA-ECC	1	0.011	0.011

Note: Average crack width = Total width of all cracks/Number of cracks.

### 3.3. Load-Displacement Curves

Due to the symmetric design of the beam–column joint specimen, only typical load-displacement curves of the right beam are plotted in Figure 9. The positive and negative loads were defined as upward loading and downward loading, respectively.

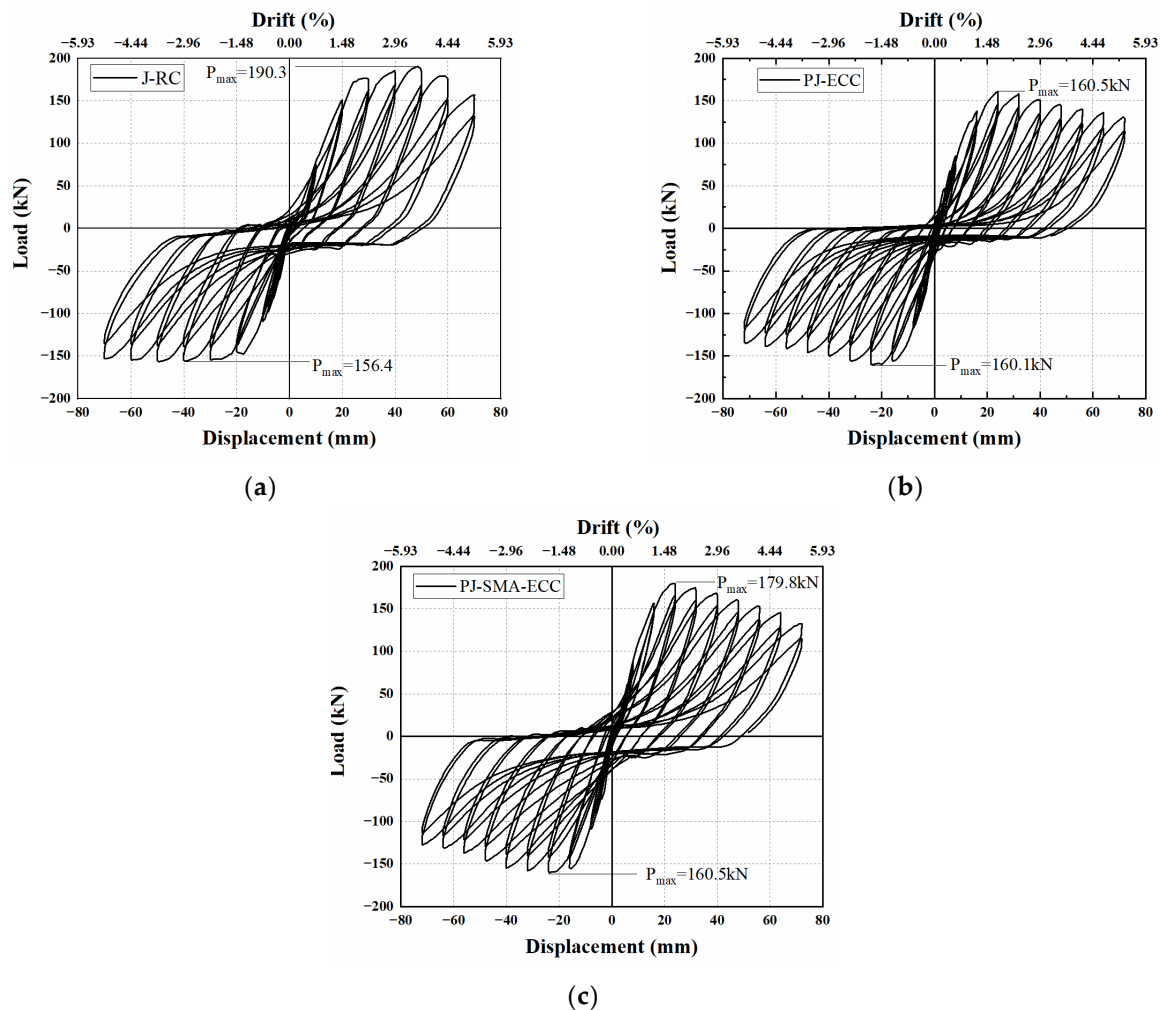


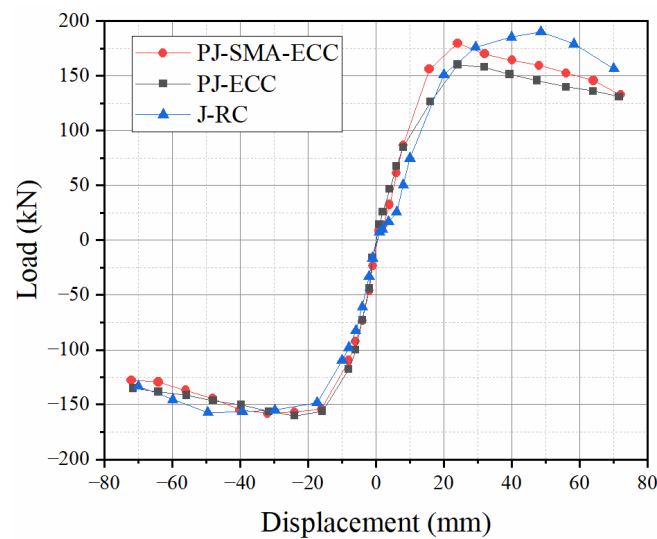
Figure 9. Hysteresis curves of specimens for (a) J-RC, (b) PJ-ECC, and (c) PJ-SMA-ECC.

Figure 9a shows that Specimen J-RC had relatively flat hysteresis loops with less pinching effect, indicating good bonding between the reinforcement and concrete. The load began to drop at a displacement of approximately 48 mm and 50 mm in the positive and negative directions. As shown in Figure 9b, Specimen PJ-ECC exhibited a stable hysteretic behavior with a few pinching effects, indicating increased slip at the interface which was caused by the vertical cracks. As shown in Figure 9c, Specimen PJ-SMA-ECC and PJ-ECC had similar hysteretic behavior. However, the hysteresis loops of Specimen PJ-SMA-ECC were fuller compared with Specimen PJ-ECC. This may be attributed to the super-elastic SMA fibers transformation caused by the “Martensite Effect” and “Austenite Effect” [46], which is beneficial for energy absorption.

Specimen PJ-SMA-ECC and Specimen J-RC had similar performance in the elastic phase. When the loading displacement reached 48 mm, Specimen J-RC reached its maximum load-carrying capacity (190.3 kN); in contrast, the maximum load-carrying capacity of Specimen PJ-SMA-ECC was only 179.8 kN. It is assumed that compared with cast-in-place RC joints, the post-casting of the precast joint caused a weak interface between pre-casted and post-casted components; thus, the interface was relatively sensitive to cyclic loads which resulted in the deterioration of the load-bearing capacity of the SMA-ECC joint specimen.

Figure 10 shows the skeleton curve of all the specimens. As shown in Figure 10, the load increased rapidly with increasing displacement, indicating that the initial stiffness of the specimen was relatively large. The skeleton curve of Specimen PJ-SMA-ECC was similar to Specimen J-RC, indicating that the SMA-ECC composite in the post-cast joint

zone had better stress and strain compatibility compared with ordinary concrete, which was beneficial to the strengthening effect of reinforcement.



**Figure 10.** Skeleton curve of the specimens.

### 3.4. Strength, Displacement, and Ductility

Table 9 lists the cracking strength  $P_c$ , yield strength  $P_y$ , peak strength  $P_m$ , ultimate strength  $P_u$ , cracking displacement  $\Delta_c$ , yield displacement  $\Delta_y$ , peak displacement  $\Delta_m$ , ultimate displacement  $\Delta_u$ , and ductility  $\mu$  of the specimens. The ultimate displacement was defined as the post-peak displacement corresponding to 85% of the peak load, while the yield displacement was determined based on the equivalent elasto-plastic energy absorption method [47]. As shown in Figure 11, the position of yield point B is determined when the area enclosed by the curve OAFO is equal to the area enclosed by the curve FCDF. Ductility is defined by Equation (4):

$$\mu = \Delta_u / \Delta_y \quad (4)$$

where  $\Delta_u$  is ultimate displacement,  $\Delta_y$  is yield displacement, and  $\mu$  is ductility.

**Table 9.** Summary of test results for specimens.

Specimen		$P_c$ (kN)	$\Delta_c$ (mm)	$P_y$ (kN)	$\Delta_y$ (mm)	$P_m$ (kN)	$\Delta_m$ (mm)	$P_u$ (kN)	$\Delta_u$ (mm)	$\mu$
J-RC	Pos.	NA	NA	175.7	29.0	190.3	48.5	161.8	67.4	2.33
	Neg.	60.8	4.0	137.5	15.3	157.0	49.5	133.5	69.8	4.56
	Average	60.8	4.0	156.6	22.2	173.7	49.0	147.7	68.6	3.45
PJ-ECC	Pos.	NA	NA	137.5	18.6	160.5	24.1	136.4	63.2	3.40
	Neg.	72.8	4.0	135.7	11.7	160.1	24.0	136.1	69.3	5.92
	Average	72.8	4.0	136.6	15.2	160.3	24.1	136.3	66.3	4.66
PJ-SMA-ECC	Pos.	NA	NA	151.2	14.9	179.8	24.0	152.8	56.0	3.76
	Neg.	73.7	4.0	121.9	10.3	158.2	32.0	134.5	57.4	5.57
	Average	73.7	4.0	136.6	12.6	169.0	28	143.7	56.7	4.67

The peak strength of Specimen J-RC was 8.4% and 2.8% greater than that of Specimens PJ-ECC and PJ-SMA-ECC, respectively, since Specimen J-RC had better integrity compared to precast joints. Cracks of all specimens were initiated at a negative displacement of 4 mm. The cracking strength of Specimens J-RC, PJ-ECC, and PJ-SMA-ECC were 60.8 kN, 72.8 kN, and 73.7 kN, respectively. Specimen J-RC exhibited the largest yield and peak strengths due to good integrity of the fully cast-in-place joint.

The ductility was 4.67 for Specimen PJ-SMA-ECC, 4.66 for Specimen PJ-ECC, and 3.45 for Specimen J-RC, as listed in Table 9. The precast joint specimens had higher ductility compared with Specimen J-RC. The ductility of Specimens PJ-SMA-ECC and PJ-ECC increased by 35% compared with Specimen J-RC. The reasons are: (i) SMA-ECC and ECC effectively improved the integrity of precast joints and (ii) the yield displacement of Specimen J-RC was larger than that of Specimens PJ-SMA-ECC and PJ-ECC, as discussed earlier.

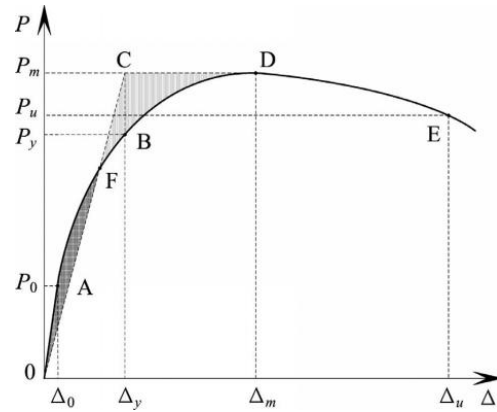


**Figure 11.** Definition of yield displacement.

### 3.5. Stiffness Degradation

The average scant stiffness for a given displacement target is calculated using Equation (5):

$$K_j = \frac{\sum_{i=1}^n P_j^i}{\sum_{i=1}^n \Delta_j^i} \quad (5)$$

where  $P_j^i$  and  $\Delta_j^i$  are the peak load and corresponding displacement at the  $i^{\text{th}}$  cycle of the displacement target  $j$ , respectively, and  $n$  is the total load cycles at each displacement level.

Stiffness is plotted against displacement in Figure 12. Stiffness decreased continuously with increasing displacement because of the accumulated damage during the test. The initial stiffness of Specimens PJ-SMA-ECC and PJ-ECC were slightly smaller than Specimen J-RC, which may be caused by the lower elastic modulus of the ECC matrix. It was observed that the stiffness degraded quickly at earlier loading cycles and the degradation rate gradually reduced after a displacement of 30 mm. After the displacement reached 24 mm, Specimen PJ-SMA-ECC exhibited a similar stiffness degradation trend as Specimen J-RC, which implied that the proposed joint has comparable seismic behavior to that of the monolithically cast concrete joint in terms of stiffness degradation.

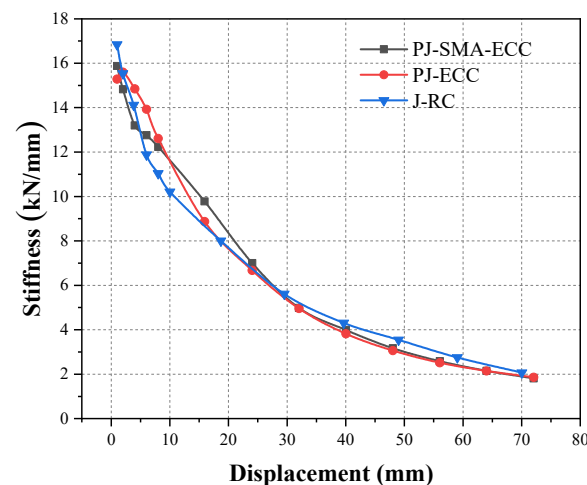


**Figure 12.** Stiffness degradation.

### 3.6. Energy Dissipation and Damping Ratio

The dissipated energy was determined by the enclosed area of the hysteretic loop in each cycle. Cumulative dissipated energy is a widely adopted parameter to assess the energy dissipation capacity of a structural member. Cumulative dissipated energy in the first cycle at each displacement target was plotted for all the specimens in Figure 13a. The dissipated energy continuously increased with increasing displacement. The three specimens exhibited a similar pattern of energy dissipation before the displacement reached 16 mm. The dissipated energy of Specimen PJ-SMA-ECC was greater than that of the other two specimens after yielding, which suggested that SMA fibers in the joint zone can effectively improve the energy dissipation capacity of the joint.

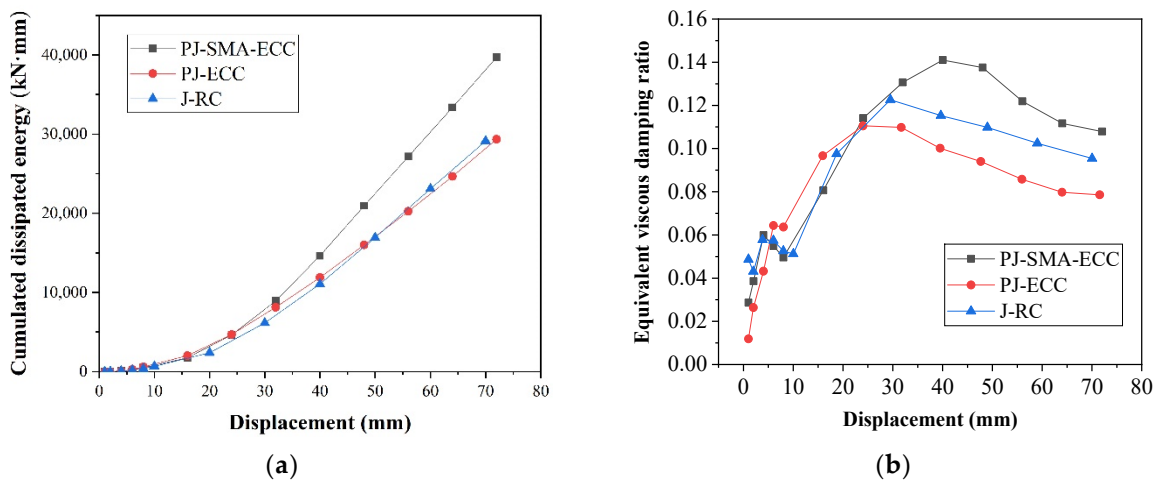


**Figure 13.** Dissipated energy for all the specimens. (a) Cumulative dissipated energy; (b) Equivalent viscous damping ratio.

The equivalent viscous damping ratio  $h_e$  was calculated by Equation (6) and plotted against displacement in Figure 13b:

$$h_e = \frac{1}{2\pi} \cdot \frac{S_{ABCD}}{S_{GOD} + S_{EOB}} \quad (6)$$

where  $S_{ABCD}$  is the energy dissipation in the load cycle defined as the area enclosed by a complete load cycle (i.e., area enclosed by curve ABCDA);  $S_{GOD}$  is the triangular area enclosed by points G, O, and D; and  $S_{EOB}$  is the triangular area enclosed by points E, O, and B. The location of these points can be referred to in Figure 14.

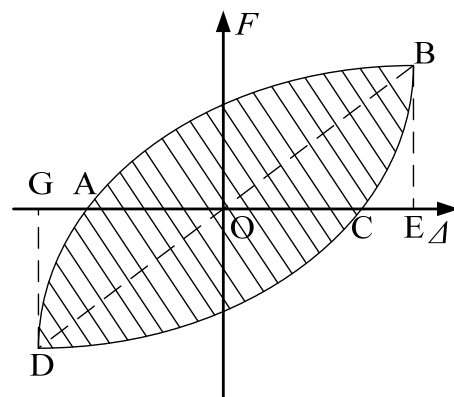


**Figure 14.** Method used to calculate the equivalent viscous damping ratio.

At the initial loading stage,  $h_e$  of Specimens PJ-SMA-ECC and PJ-ECC were lower than Specimen J-RC. In the yielding stage,  $h_e$  for all the specimens was approximately 0.05. When the displacement increased to 24 mm,  $h_e$  for Specimen PJ-ECC was higher than the other two specimens. Specimen PJ-SMA-ECC had a similar trend to Specimen J-RC, as shown in Figure 13b. The maximum value of  $h_e$  of Specimen PJ-SMA-ECC reached 0.14, which was 33.3% and 16.7% higher than Specimens PJ-ECC and J-RC, respectively. With a further increase in displacement, the  $h_e$  values for all specimens decreased because of the slip of longitudinal bars or joint failure [23]. By the end of the test,  $h_e$  for Specimen PJ-SMA-ECC was still higher than Specimen J-RC. Specimen PJ-SMA-ECC exhibited better energy dissipation capacity compared with the other two specimens due to superior energy dissipation capacity and damage resistance of the SMA-ECC material.

#### 4. Evaluation of Self-Healing Performance

##### 4.1. Maximum Crack Width at Each Cycle before and after Unloading

The maximum crack width is a direct indicator to evaluate the crack self-healing ability of the joints. Crack width was measured when the specimen was loaded to each target displacement and after unloading with a crack gauge, and it was measured again after the entire test ended. Cracks in the joint zone of the three specimens were initiated when the specimen yielded. The maximum crack width of all specimens before and after unloading of each cycle in the joint zone is compared in Figure 15. As shown in Figure 15a, the crack width of Specimen J-RC increased rapidly with increasing displacement and the maximum crack width was 1.128 mm when the displacement reached 70 mm. The crack width of Specimen PJ-ECC also increased with increasing displacement, but the width of the maximum crack was noticeably smaller than that of Specimen J-RC under the same beam end load. This may be attributed to the bridging effect of PVA fibers which can effectively control the development and propagation of cracks. After unloading, the maximum crack width decreased slightly for both Specimens J-RC and PJ-ECC, showing poor crack self-healing in the two joints (black line in Figure 15a,b). The closure of partial cracks was triggered by the “spring effect” of small cracks after unloading, which is not the self-healing ability of the joint itself. However, the fully closed crack in Specimen PJ-SMA-ECC was observed, with the maximum crack width only reaching 0.043 mm (red line in Figure 15b). The crack closing ratio  $R$  is defined by Equation (7):

$$R = \frac{w_{\max,i} - w_t}{w_{\max,i}} \quad (7)$$

where  $w_{\max,i}$  is the maximum crack width when the specimen was loaded to each target displacement and  $w_t$  is the crack width after unloading.

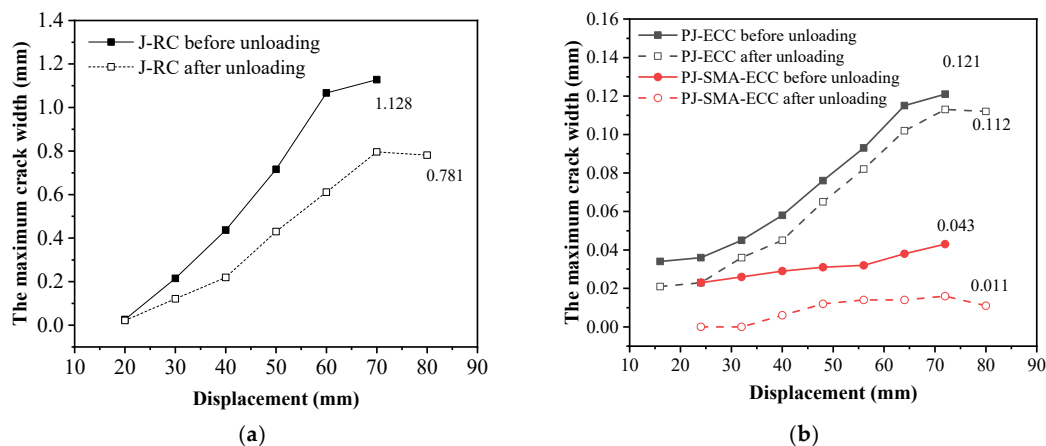


**Figure 15.** The maximum crack width before and after unloading of each cycle load for specimens. Note: The crack widths of specimens J-RC, PJ-ECC, and PJ-SMA-ECC with a displacement of 80 mm are measured fifteen minutes after the test ended. (a) J-RC; (b) PJ-ECC and PJ-SMA-ECC.

The crack closing ratio of all the specimens is plotted in Figure 16. Compared with the other two specimens, Specimen PJ-SMA-ECC exhibited superior crack self-healing ability. That is because the super-elastic SMA fibers can automatically repair cracks after unloading. At the early stage of loading, the cracks in the joint zone of Specimen PJ-SMA-ECC were almost completely closed. However, the crack width gradually increased and the crack closing ratio decreased to 60% with increasing displacement. This may have resulted from the limitation of self-healing efficiency of the SMA-ECC materials caused by increasing crack width [48]. Fifteen minutes after the entire test ended, the  $R$  of PJ-SMA-ECC had a slight increase; this is probably because the super-elastic effect of SMA fibers needs a buffer time to maximize its self-healing capacity after unloading.

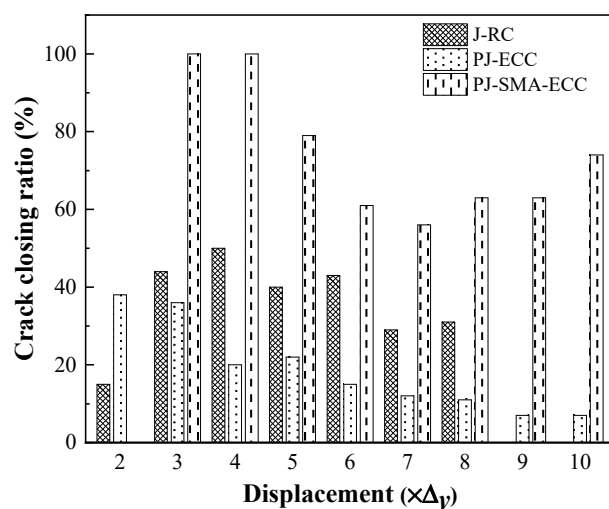


**Figure 16.** The crack closing ratio in the joint zone.

## 4.2. Ultrasonic Pulse Test

### 4.2.1. Testing Method

The ultrasonic pulse test is an effective method for detecting internal defects and damages to concrete/cementitious materials by non-metallic ultrasonic pulse instruments [49]. To further analyze and compare the self-healing performance of Specimens PJ-ECC and PJ-SMA-ECC, an ultrasonic detector with a pair of ultrasonic transducers was used to perform this test in the joint zone. The detector uses an ultrasonic wave introduced by a transmitter into concrete. The generated ultrasonic wave, after traversing through the joint, is finally detected by a receiver to measure the travelling time, speed, and amplitude of the ultrasonic wave. These parameters of the acoustic wave exhibited observable variation when traveling through cracks generated in the joint compared with intact matrix. The measured acoustic speed and amplitude will decrease once they pass through cracks. In other words, the damage of joints can be determined by the variation of the aforementioned acoustic parameters.

Ultrasonic pulse tests were conducted on Specimens PJ-ECC and PJ-SMA-ECC at different stages: before loading, at each target displacement, and after unloading. Initial acoustic speed and amplitude, and measured acoustic speed and amplitude at each target displacement and after unloading were collected, respectively. Each target displacement is listed in Table 10. Details of the numbering of measurements at different stages are shown in Table 10. The number 0 corresponds to the initial measurement before loading. Numbers from 1 to 22 correspond to measurements when the specimen was loaded to each target displacement. Numbers 23, 24, and 25 correspond to measurements conducted at 15 min, 60 min, and 24 h after the entire loading process, respectively.

**Table 10.** Definition of the numbering of measurements.

	Before Test			During Test				After Test		
Number	1	2	3	4	5	6	7	23	24	25
Target displacement	Initial	$2\Delta_y$	0	$-2\Delta_y$	$3\Delta_y$	0	$-3\Delta_y$	15 min	60 min	24 h

Two parallel sides of the joint zone were selected for ultrasonic inspection. A grid was drawn with a spacing of 80 mm orthogonally on both sides, with detection points marked as 1 to 36. The transmitter was installed on one side and the receiver was installed on the other side. To maximize the coupling effect, an appropriate coupling agent was applied on their surface before installation. The test method is similar to those previously performed by the authors [39].

#### 4.2.2. Variation in Acoustic Speed and Amplitude before and after Unloading

During the ultrasonic pulse test, the variation in acoustic speed and amplitude of Specimens PJ-SMA-ECC and PJ-ECC was compared, as shown in Figure 17. It can be seen that the initial acoustic speed and amplitude of PJ-SMA-ECC and PJ-ECC are the same, indicating the consistency in the initial damage of the two types of precast joints. With the increase of loading displacement, the acoustic speed and amplitude decreased due to increasing damage inside the specimen. In fact, this finding is consistent with the authors' previous finding reported in [39].

From Figure 17a, compared to Specimen PJ-SMA-ECC, there was a sharp decline of acoustic speed for Specimen PJ-ECC at a target displacement of  $2\Delta_y$ . When the specimens failed (corresponding to measurement number 22), the acoustic speed of Specimens PJ-SMA-ECC and PJ-ECC decreased to 72.2% and 48.9% of the initial acoustic speed, respectively. It indicated that Specimen PJ-ECC suffered greater damage. It may be attributed to the fact that SMA-ECC materials have higher damage tolerance compared to ECC materials. In addition, the recovery of acoustic speed after unloading decreased with the increase of displacement, especially for Specimen PJ-ECC. The slight recovery of acoustic speed for Specimen PJ-ECC may be due to the "spring effect" of PVA fibers. In contrast, Specimen PJ-SMA-ECC exhibited excellent damage-recovery properties after an earthquake. For example, the acoustic speed of Specimen PJ-SMA-ECC recovered to 91.3% of its initial acoustic speed 15 min after the end of the entire loading process (i.e., measurement number 23).

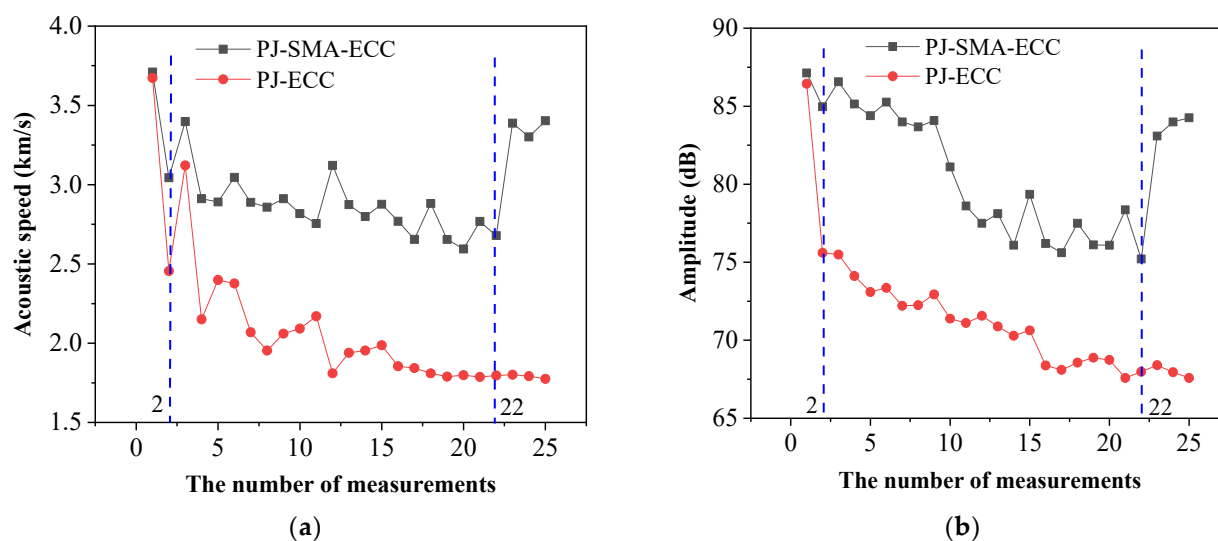


**Figure 17.** The variation in the acoustic speed and amplitude of specimens PJ-SMA-ECC and PJ-ECC. (a) The variation in acoustic speed; (b) The variation in amplitude.

For a visual comparison of the damage-recovery capacity after an earthquake, the damage-recovery rate  $R_d$  is defined by Equation (8):

$$R_d = \frac{A_{23} - A_{22}}{A_1 - A_{22}}. \quad (8)$$

where  $A_1$  is the initial acoustic speed/amplitude;  $A_{22}$  is the acoustic speed/amplitude before self-healing (at the end of the entire loading test with measurement number 22); and  $A_{23}$  is the acoustic speed/amplitude after self-healing (15 min after unloading with measurement number 23).

The comparison of the damage-recovery rate between Specimens PJ-ECC and PJ-SMA-ECC is shown in Figure 18. It can be seen that, in terms of acoustic speed, Specimen PJ-SMA-ECC had a noticeable recovery with a damage-recovery rate of 69.2%, which reflected good self-healing properties. However, there was barely recovery of control specimen PJ-ECC. It suggests that the “austenite effect” of super-elastic SMA fibers can be fully utilized after unloading. In fact, this finding is similar with the crack results discussed in Section 4.1. The variation and recovery rate of amplitude were similar to that of the acoustic speed, with no further discussion proposed.

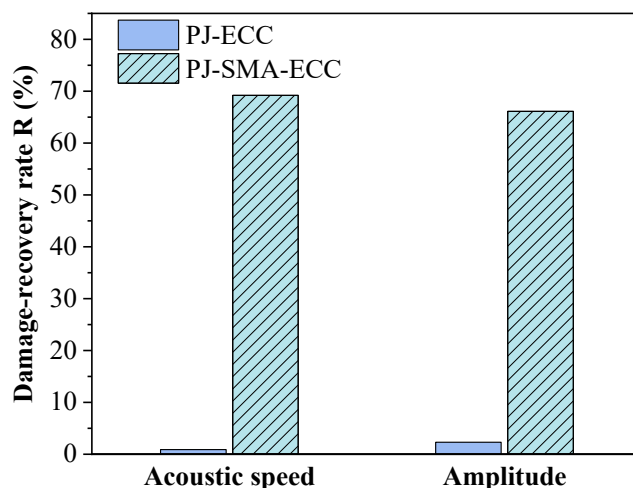


Figure 18. The comparison of the damage-recovery rate.

The ultrasonic pulse test indicated that the use of SMA-ECC materials in the joint zone is effective in crack repairing and internal damage recovery. Therefore, the proposed joint has promising performance in regions with high seismicity, which can soon repair its cracks and damage, and considerably reduce post-earthquake repair and retrofitting efforts.

## 5. Conclusions

This study experimentally investigated the seismic behavior and the post-earthquake self-healing performance of an innovative precast joint using SMA-ECC materials. Based on the experimental results, the following conclusions were obtained:

- (1) The seismic performance of Specimen PJ-SMA-ECC was comparable to (even better in certain aspects, such as the ability to maintain structural integrity, displacement ductility, and energy dissipation capacity) the monolithically cast Specimen J-RC. The two precast joints experienced flexural failure at the beam ends and maintained good integrity at failure.
- (2) Specimen PJ-SMA-ECC exhibited superior crack-healing capacity by reducing the crack number and width. Almost all cracks in the joint zone of Specimen PJ-SMA-ECC were closed after the test was terminated. Super-elastic SMA fibers were beneficial in repairing cracks after load removal.

- (3) An ultrasonic pulse test showed that the acoustic speed and amplitude of Specimen PJ-SMA-ECC decreased slowly with increasing displacement. Additionally, the acoustic speed and amplitude in the joint zone of Specimen PJ-SMA-ECC recovered to 91.3% and 96.7% of their initial values after the test was terminated, while the acoustic properties of Specimen PJ-ECC were barely recovered.

This paper presents only a preliminary experimental investigation of the seismic performance of precast self-healing beam–column joints using SMA-ECC materials in the joint core zone. The goal of this study is to validate the feasibility of the following two points: (i) The seismic performance of the precast beam–column joint with SMA-ECC materials is comparable to the monolithically cast joint with conventional concrete; (ii) The application of innovative SMA-ECC self-healing materials in the joint core zone can enhance the energy dissipation capacity and self-healing ability, and significantly reduce the crack width and damage, and realize the rapid repair and recovery in cracks and damage respectively after earthquakes. However, further work needs to be conducted. In our next research, we will focus on numerical simulation and theoretical analysis to gain a better understanding of the seismic behaviors of precast self-healing beam–column joints reinforced with SMA-ECC materials.

**Author Contributions:** Conceptualization, W.C.; investigation, W.C., K.F. and S.C.; resources, W.C.; funding acquisition, W.C.; methodology, K.F.; data curation, K.F. and S.C.; writing—original draft preparation, K.F.; validation, Y.W.; writing—review and editing, Y.W.; project administration, Y.L. All authors have read and agreed to the published version of the manuscript.

**Funding:** This study was funded by the Scientific Research Founding of Key Laboratory of Building Collapse Mechanism and Disaster Prevention, China Earthquake Administration (Grant No. FZ211106).

**Institutional Review Board Statement:** “Not applicable” for these studies not involving humans or animals.

**Informed Consent Statement:** “Not applicable” for these studies not involving humans.

**Data Availability Statement:** The data presented in this study are available on request from the corresponding author. The data are not publicly available due to privacy.

**Conflicts of Interest:** All authors declare that they have no conflict of interest.

## References

- Kurama, Y.C.; Sritharan, S.; Fleischman, R.B.; Restrepo, J.I.; Henry, R.S.; Cleland, N.M.; Ghosh, S.K.; Bonelli, P. Seismic-resistant precast concrete structures: State of the art. *J. Struct. Eng.* **2018**, *144*, 03118001. [[CrossRef](#)]
- Yan, Q.; Chen, T.; Xie, Z. Seismic experimental study on a precast concrete beam–column connection with grout sleeves. *Eng. Struct.* **2018**, *155*, 330–344. [[CrossRef](#)]
- Palanci, M.; Senel, S.M. Earthquake damage assessment of 1-story precast industrial buildings using damage probability matrices. *B Earthq. Eng.* **2019**, *17*, 5241–5263. [[CrossRef](#)]
- Belleri, A.; Brunesi, E.; Nascimbene, R.; Pagani, M.; Riva, P. Seismic performance of precast industrial facilities following major earthquakes in the Italian territory. *J. Perform. Constr. Fac.* **2015**, *29*, 04014135. [[CrossRef](#)]
- Xu, Y.L.; Gong, Y.N. Investigation of collapse of teaching building during the Wenchuan Earthquake: Third anniversary memorial of 5·12 Wenchuan Earthquake. *J. Build Struct.* **2011**, *32*, 9–16. (In Chinese)
- Bruneau, M. Building damage from the Marmara, Turkey Earthquake of August 17, 1999. *J. Seismol.* **2002**, *6*, 357–377. [[CrossRef](#)]
- Senel, S.M.; Palanci, M.; Kalkan, A.; Yilmaz, Y. Investigation of shear and overturning safety of hinged connections in existing precast buildings. *Tek. Dergi.* **2013**, *24*, 6505–6528.
- Bazant, Z.P.; Kazemi, M.T. Size dependence of concrete fracture energy determined by RILEM work-of-fracture method. *Int. J. Fract.* **1991**, *51*, 121–138. [[CrossRef](#)]
- Khan, M.S. Seismic performance of deficient RC frames retrofitted with SMA-reinforced ECC column jacketing. *Innov. Infrastruct. Solut.* **2021**, *6*, 1–20. [[CrossRef](#)]
- Şahmaran, M.; Li, V. De-icing salt scaling resistance of mechanically loaded engineered cementitious composites. *Cem. Concr. Res.* **2007**, *37*, 1035–1046. [[CrossRef](#)]
- Yu, K.; Li, L.; Yu, J.; Wang, Y.; Ye, J.; Xu, Q. Direct tensile properties of engineered cementitious composites: A review. *Constr. Build. Mater.* **2018**, *165*, 346–362. [[CrossRef](#)]

12. Haber, Z.B.; De la Varga, I.; Graybeal, B.A.; Nakashoji, B.; El-Helou, R. *Properties and Behavior of UHPC-Class Materials*; FHWA-HRT-18-036; Federal Highway Administration, Office of Infrastructure Research and Development: McLean, VA, USA, 2018.
13. Shao, Y.; Nguyen, W.; Bandelt, M.J.; Ostertag, C.P.; Billington, S.L. Seismic performance of high-performance fiber-reinforced cement-based composite structural members: A review. *J. Struct. Eng.* **2022**, *148*, 03122004. [[CrossRef](#)]
14. Pokhrel, M.; Bandelt, M.J. Plastic hinge behavior and rotation capacity in reinforced ductile concrete flexural members. *Eng. Struct.* **2019**, *200*, 109699. [[CrossRef](#)]
15. Shao, Y.; Hung, C.C.; Billington, S.L. Gradual crushing of steel reinforced HPFRCC beams, experiments and simulations. *J. Struct. Eng.* **2021**, *147*, 04021114. [[CrossRef](#)]
16. Kesner, K.E.; Billington, S.L.; Douglas, K.S. Cyclic response of highly ductile fiber-reinforced cement-based composites. *ACI Mater. J.* **2003**, *100*, 381–390.
17. Khlef, F.L.; Barbosa, A.R.; Ideker, J.H. Tension and cyclic behavior of high-performance fiber-reinforced cementitious composites. *J. Mater. Civil Eng.* **2019**, *31*, 04019220. [[CrossRef](#)]
18. Del Vecchio, C.; Di Ludovico, M.; Balsamo, A.; Prota, A. Seismic retrofit of real beam-column joints using fiber-reinforced cement composites. *J. Struct. Eng.* **2018**, *144*, 04018026. [[CrossRef](#)]
19. Filiatrault, A.; Pineau, S.; Houde, J. Seismic behavior of steel-fiber reinforced-concrete interior beam-column joints. *ACI Struct. J.* **1995**, *92*, 543–552.
20. Zhang, Z.; Ding, R.; Nie, X.; Fan, J. Seismic performance of a novel interior precast concrete beam-column joint using ultra-high performance concrete. *Eng. Struct.* **2020**, *222*, 111145. [[CrossRef](#)]
21. Parra-Montesinos, G.J.; Peterfreund, S.W.; Chao, S.H. Highly damage-tolerant beam-column joints through use of high-performance fiber-reinforced cement composites. *ACI Struct. J.* **2005**, *102*, 487–495.
22. Qudah, S.; Maalej, M. Application of engineered cementitious composites (ECC) in interior beam-column connections for enhanced seismic resistance. *Eng. Struct.* **2014**, *69*, 235–245. [[CrossRef](#)]
23. Gou, S.; Ding, R.; Fan, J.; Nie, X.; Zhang, J. Seismic performance of a novel precast concrete beam-column connection using low-shrinkage engineered cementitious composites. *Constr. Build. Mater.* **2018**, *192*, 643–656. [[CrossRef](#)]
24. Gou, S.; Ding, R.; Fan, J.; Nie, X.; Zhang, J. Experimental study on seismic performance of precast LSECC/RC composite joints with U-shaped LSECC beam shells. *Eng. Struct.* **2019**, *189*, 618–634. [[CrossRef](#)]
25. Ismail, M.K.; Abdelaleem, B.H.; Hassan, A.A. Effect of fiber type on the behavior of cementitious composite beam-column joints under reversed cyclic loading. *Constr. Build. Mater.* **2018**, *186*, 969–977. [[CrossRef](#)]
26. Tazarv, M.; Saiid, M. Low-damage precast columns for accelerated bridge construction in high seismic zones. *J. Bridge Eng.* **2016**, *21*, 04015056. [[CrossRef](#)]
27. Mahmoud, M.A.E.; Nehdi, M.L. Exploring the synergy of ECCs and SMAs in creating resilient civil infrastructure. *Mag. Concr. Res.* **2018**, *70*, 172–188. [[CrossRef](#)]
28. Del Vecchio, C.; Di Ludovico, M.; Pampanin, S.; Prota, A. Repair costs of existing RC buildings damaged by the L'Aquila earthquake and comparison with FEMA P-58 predictions. *Earthq. Spectra.* **2018**, *34*, 237–263. [[CrossRef](#)]
29. Baker, T.; Saiidi, M.S.; Nakashoji, B.; Bingle, J.; Moore, T.; Khaleghi, B. Precast concrete spliced-girder bridge in Washington State using superelastic materials in bridge columns to improve seismic resiliency, From research to practice. *PCI J.* **2018**, *63*, 57–71. [[CrossRef](#)]
30. Ghodke, S.; Jangid, R.S. Influence of high austenite stiffness of shape memory alloy on the response of base isolated benchmark building. *Struct. Control. Health.* **2017**, *24*, e1867. [[CrossRef](#)]
31. Li, X.; Li, M.; Song, G. Energy-dissipating and self-repairing SMA-ECC composite material system. *Smart Mater. Struct.* **2015**, *24*, 025024. [[CrossRef](#)]
32. Qian, H.; Zhang, Q.; Zhang, X.; Deng, E.; Gao, J. Experimental investigation on bending behavior of existing RC beam retrofitted with SMA-ECC composites materials. *Materials* **2021**, *15*, 12. [[CrossRef](#)] [[PubMed](#)]
33. Varela, S.; Saiidi, M. Dynamic performance of innovative bridge columns with superelastic Cu-Al-Mn shape memory alloy and ECC. *Int. J. Bridge Eng.* **2014**, *1*, 29–58.
34. Hosseini, F.; Gencturk, B.; Lahpour, S.; Gil, D.I. An experimental investigation of innovative bridge columns with engineered cementitious composites and Cu-Al-Mn super-elastic alloys. *Smart Mater. Struct.* **2015**, *24*, 085029. [[CrossRef](#)]
35. Cruz Noguez, C.A.; Saiidi, M.S. Shake-table studies of a four-span bridge model with advanced materials. *J. Struct. Eng.* **2012**, *138*, 182–191. [[CrossRef](#)]
36. Qian, H.; Li, Z.; Pei, J.; Kang, L.; Li, H. Seismic performance of self-centering beam-column joints reinforced with superelastic shape memory alloy bars and engineering cementitious composites materials. *Compos Struct.* **2022**, *294*, 115782. [[CrossRef](#)]
37. Ali, M.A.E.M.; Nehdi, M.L. Innovative crack-healing hybrid fiber reinforced engineered cementitious composite. *Constr. Build. Mater.* **2017**, *150*, 689–702. [[CrossRef](#)]
38. Ali, M.A.E.M.; Soliman, A.M.; Nehdi, M.L. Hybrid-fiber reinforced engineered cementitious composite under tensile and impact loading. *Mater. Des.* **2017**, *117*, 139–149. [[CrossRef](#)]
39. Chen, W.; Feng, K.; Wang, Y.; Lin, Y.; Qian, H. Evaluation of self-healing performance of a smart composite material (SMA-ECC). *Constr. Build. Mater.* **2021**, *290*, 123216. [[CrossRef](#)]
40. Chen, W.; Lin, B.; Feng, K.; Cui, S.; Zhang, D. Effect of shape memory alloy fiber content and preloading level on the self-healing properties of smart cementitious composite (SMA-ECC). *Constr. Build. Mater.* **2022**, *341*, 127797. [[CrossRef](#)]

41. GB 50011-2010; Code for Seismic Design of Buildings. China Architecture and Building Press: Beijing, China, 2010. (In Chinese)
42. ACI 352R-02; Recommendations for Design of Beam–Column Connections in Monolithic Reinforced Concrete Structures. American Concrete Institute: Farmington Hills, MI, USA, 2002.
43. GB/T 50081-2019; Standard for Test Methods of Concrete Physical and Mechanical Properties. China Building Industry Press: Beijing, China, 2019. (In Chinese)
44. GB/T 228.1-2010; Metallic Materials-Tensile Testing-Part 1: Method of Test at Room Temperature. China Standardization Administration: Beijing, China, 2010. (In Chinese)
45. JGJ/T 101-2015; Specification for Seismic Test of Building. China Architecture and Building Press: Beijing, China, 2015. (In Chinese)
46. Li, Y.; Cui, L.; Zheng, Y.; Yang, D. Reverse martensitic transformation of prestrained TiNi shape memory alloy in cement composite. *J. Mater. Sci. Lett.* **2001**, *22*, 1685–1686. [[CrossRef](#)]
47. Park, R. Valuation of ductility of structures and structural assemblages from laboratory testing. *Bull. N. Z. Nat. Soc. Earthq. Eng.* **1989**, *22*, 155–166.
48. Kim, V.T.; Nele, D.B. Self-healing in cementitious materials—A review. *Materials* **2013**, *6*, 2182–2217.
49. Zhu, Y.; Yang, Y.; Yao, Y. Autogenous self-healing of engineered cementitious composites under freeze–thaw cycles. *Constr. Build. Mater.* **2012**, *34*, 522–530. [[CrossRef](#)]